Journal of Environmental Chemical Engineering 10 (2022) 107389

Contents lists available at ScienceDirect

Journal of Environmental Chemical Engineering

journal homepage: www.elsevier.com/locate/jece

Comparative and competitive adsorption of gaseous toluene, ethylbenzene, and xylene onto natural cellulose-modified Fe_3O_4 nanoparticles

Mehmet Şakir Ece [a], Sinan Kutluay [b,*]

[a] Vocational High School of Health Services, Mardin Artuklu University, 47100 Mardin, Turkey
[b] Department of Chemical Engineering, Faculty of Engineering, Siirt University, 56100 Siirt, Turkey

ARTICLE INFO

Editor: V. Victor

Keywords:
Competitive adsorption
Toluene/ethylbenzene/xylene
Natural cellulose-modified Fe_3O_4 nanoparticles
Volatile organic compounds
Reuse efficiency/regeneration

ABSTRACT

Many industrial processes produce volatile organic compound (VOC) pollutants within multicomponent systems. Therefore, exploring the comparative and competitive adsorption of VOCs is of both practical and scientific interest. This study elucidates the adsorption behavior of gaseous toluene, ethylbenzene, and xylene (TEX) targeted as VOCs onto natural cellulose-modified Fe_3O_4 (NC-Fe_3O_4) nanoparticles (NPs) both individually and in multicomponent systems for the first time in the literature. The characterization of NC-Fe_3O_4 synthesized via co-precipitation method was carried out with analysis techniques including BET, SEM, EDS, FTIR, and TGA-DTA. The adsorption capacities of TEX as a single-component onto NC-Fe_3O_4 (for 20 mg L^{-1} TEX inlet concentration) were found as 477, 550, and 578 mg g^{-1}, respectively. In contrast, with TEX in a binary-component system, the adsorption capacity of the T (for 20 mg L^{-1} T with 10 mg L^{-1} E and 10 mg L^{-1} X, respectively) decreased by approximately 43% and 50% for the binary-mixtures of T-E and T-X, respectively, due to competition with E and X for adsorption sites. Similarly, the adsorption capacity of the E (for 20 mg L^{-1} E with 10 mg L^{-1} X) decreased by approximately 46% due to competition with the X for adsorption sites. With TEX in a ternary-component system, the adsorption capacity of the X remained consistent, indicating its competitive dominance over the E and T. The adsorption capacity of NC-Fe_3O_4 followed the order of X > E > T in the ternary-component system, which agrees with the adsorption results for the single-component system. The adsorption mechanism of TEX was explained by fitting the adsorption data to diverse kinetic and isotherm models. The NC-Fe_3O_4 with a superior performance in terms of both reuse efficiency and adsorption capacity, could be used as a promising and renewable adsorbent for efficient treatment of VOC pollutants. The findings of the current study will contribute to a better understanding of the comparative and competitive adsorption behaviors among different VOC pollutants in relation to a given adsorbent.

1. Introduction

Besides consuming natural resources, the world's constantly increasing industrialization and urbanization processes, such as those in the areas of transportation, manufacturing, construction, oil refining, and mining, also produce large amounts of hazardous wastes that cause air, water, and soil pollution and consequently threaten human health and environmental safety. The produced wastes are released into the environment in different ways. For instance, soil and water pollutants contain organic substances (e.g., pesticides, pesticides, phenols, and hydrocarbons) and heavy metals (e.g., lead, cadmium, arsenic, and mercury), as well as microbial pathogens, while atmospheric pollutants contain toxic gases (e.g., nitrogen oxides, sulfur oxides, carbon oxides, and ozone), airborne particles, and volatile organic compounds (VOCs) [1,2]. Air pollution is one of the most critical problems of the world, defined as the change in the natural composition of the atmosphere related to chemical, physical, or biological substances [1]. As a fundamental source of air pollution, VOCs have been on the agenda of scientists and legislators for the last two decades. Defined as a subtype of biogenic or anthropogenic compounds, VOCs are classified as the primary group of hazardous substances and air pollutants. These compounds not only exacerbate ozone depletion and the greenhouse effect but also lead to crucial harm to human health and result in irreversible damage in the event of prolonged exposure. Commonly found in crude oil and its derivatives, toluene, ethylbenzene, and xylene (TEX) are monoaromatic VOCs of health and environmental concern. The US

* Corresponding author.
E-mail address: sinankutluay@siirt.edu.tr (S. Kutluay).

https://doi.org/10.1016/j.jece.2022.107389
Received 21 September 2021; Received in revised form 9 February 2022; Accepted 11 February 2022
Available online 12 February 2022

Environmental Protection Agency has designated TEX as group A human carcinogens. In order to remove VOCs from the atmosphere, diverse separation technologies have been developed including adsorption, absorption, condensation, catalytic oxidation, photocatalytic reaction, and membrane separation. While each technique has its own advantages, adsorption is regarded as the most economical, energy-efficient, and useful due to its durability [3–8]. Competitive adsorption is a common process in multicomponent adsorption applications. Determining the competitive adsorption behavior of a developed adsorbent is very important industrially. As the number of different compounds to be treated simultaneously is increased, the competitive adsorption process becomes more complex. Compared to VOCs with low polarity, VOCs with high polarity are known to have stronger adsorption affinity with polar surface adsorbents. Furthermore, the notable ability of VOCs to occupy adsorption sites in the competitive adsorption process is caused by their high molecular weight and high boiling points [9]. Adsorption applications with more than one component are usually macroscopic. In contrast to previous studies of the adsorption of single-component VOCs, it has become common to investigate the competitive adsorption of multicomponent VOCs on adsorbents in recent years [10,11].

Nanotechnology is leading the development of new products with different functions and enormous potential in various applications. Manufactured nanomaterials can be used to solve challenging problems that cannot be addressed with conventional technologies. They have an important role in the development of innovative methods to produce new high-performance materials and chemicals that consume less energy to replace current tools. Nanoparticles (NPs) exhibit entirely new characteristics enabling them to behave more reactively than the bulk forms of the same materials. Nanoscience and nanotechnology have the potential to provide solutions or great improvements regarding most current problems, including air quality, by utilizing nanoscale adsorbents called nano-adsorbents [12,13]. Magnetite (Fe_3O_4) magnetic NPs are known to be more advantageous [(i) easy to use and prepare, and economical; (ii) versatile functionalizability, and (iii) easy to recover by means of an external magnetic field] compared to other nanomaterials [14]. Since Fe_3O_4, with versatile functionalizability, is not toxic, it has been investigated extensively as an adsorbent. This compound is prepared by means of the precipitation method, yielding high efficiency and good atom economy. As a magnetic adsorbent, Fe_3O_4 performs better than other adsorbents, particularly in removals. The properties such as high average pore diameter and total pore volume of Fe_3O_4 NPs render them noteworthy materials for adsorption applications. Furthermore, their highly reactive surface area and structural bonds also serve significant functions in adsorption. Nevertheless, the occurrence of agglomeration events during the preparation of Fe_3O_4 NPs may lead to a decrease in the number of adsorption active sites. One method to prevent particle aggregation is coating with organic or inorganic surfactants. The functional-group functionalization of Fe_3O_4 NPs not only reduces agglomeration but also generates new active sites for adsorption [13,15].

Polymer-based nanocomposites have drawn growing interest over the last two decades due to their synergistic and hybrid properties imparted by their individual components. Bio-based nanocomposites represent a new concept for ecological, bio-inspired, and functional hybrid materials composed by the combination of natural polymers and inorganic solids with at least one dimension at the nanometer scale. These bio-hybrid materials exhibit the enhanced structural and functional properties of conventional nanocomposites obtained from synthetic polymers while simultaneously offering the paramount advantages of biocompatibility, biodegradability, and certain functional properties provided by biological or inorganic moieties. Cellulose as an intriguing biopolymer and sustainable raw material can be reproduced and/or derivatized in order to develop various useful products due to its renewability, biodegradability, and derivatizability. Considering their strong intermolecular and intramolecular hydrogen bonds, nanocomposites of cellulose and its derivatives have become prominent due to their value-added applications in science and technology [16].

In this study, a cost-efficient and promising nanomagnetic adsorptive material (NC-modified Fe_3O_4) was developed by using shells of Derik Halhali olive pits as a source of natural cellulose (NC) to elucidate the competitive adsorption behavior of gaseous TEX. This aspect of our research provides a novel approach for the relevant literature. Herein, the comparative and competitive adsorption properties of various combinations of TEX in single-, binary-, and ternary-component systems onto NC-Fe_3O_4 are investigated. The adsorption mechanism of TEX is comprehensively analyzed by fitting the experimental adsorption data with various kinetic and isotherm models. Furthermore, five consecutive adsorption-desorption cycle tests are carried out on NC-Fe_3O_4 for TEX and their reuse efficiency are thus determined.

2. Materials and methods

2.1. Chemicals and reagents

Toluene ($C_5H_6CH_3$), ethylbenzene ($C6H_5CH_2CH_3$), and xylene ($C_6H_4(CH_3)_2$) were purchased from Sigma-Aldrich (St. Louis, MO, USA). Iron(III) chloride hexahydrate ($FeCl_3.6\ H_20$) and iron(II) chloride tetrahydrate ($FeCl_2.4\ H_20$) were supplied by Merck Chemical Company and Alfa Aesar Chemical Company, respectively. The chemicals and solvents applied in this study were of analytical purity. Natural cellulose was procured with the grinding of Derik Halhali olive fruits. The collected Derik Halhali olive pits were first washed with distilled water and then dried at 60 °C for 10 h. The dried olive pits were crushed and the oily parts of the pits was removed, and the shells of the pits were washed again with distilled water and then dried at 60 °C for 10 h. The shells of the obtained olive pits were used as a natural source of cellulose after grinding (350/500 mesh).

2.2. Synthesis of NC-Fe_3O_4

To synthesize NC-Fe_3O_4, the NC solution was prepared by placing 350 mg of NC into a flask containing 10 mL of deionized water under argon gas and intensely stirring the solution for 30 min at room temperature. $FeCl_3.6\ H_2O$ (940 mg, 4 mmol) and $FeCl_2.4\ H_2O$ (390 mg, 2 mmol) were added to the NC solution so that the Fe:NC ratio was 1:1. This solution was stirred at 1000 rpm and 80 °C for 30 min. To ensure coprecipitation, 5 mL of NH_3 (8 M) was added to the solution and the process yielded a change of the solution's color from orange to black. Stirring was continued for an additional 30 min. NC-Fe_3O_4 was consequently generated and separated from the solution by means of a magnet. In order to purge the NC-Fe_3O_4 of unreacted chemicals, ethanol and distilled water were alternately applied to wash it 5 times. The NC-Fe_3O_4 was then dried at 60 °C for 10 h in a drying oven [17]. The synthesized NC-Fe_3O_4 was stored in a closed amber glass bottle at room temperature and atmospheric pressure to be used for studies of the comparative and competitive adsorption of TEX.

2.3. Characterizations

The synthesized NC-Fe_3O_4 was characterized by means of different spectroscopic methods. A JEOL/JSM-6610 and Oxford Instruments/INCA X-Act were used for surface characterizations by scanning electron microscopy (SEM) images and energy-dispersive spectroscopy (EDS) measurements, respectively. Fourier transform infrared spectroscopy (FTIR) spectra were recorded with a PerkinElmer 100 FTIR spectrometer. Thermogravimetric analysis (TGA) and differential thermal analysis (DTA) thermograms were obtained from ambient temperature to 900 °C at a heating rate of 10 °C min^{-1} under N_2 atmosphere using a Shimadzu DTG-60 instrument. A Quantachrome instrument was used to measure the surface area, N_2 adsorption-desorption on NC-Fe_3O_4 at 77 K, and pore size distribution of NC-Fe_3O_4 according to the Brunauer-Emmett-Teller (BET) method.

2.4. Dynamic adsorption/desorption of TEX onto NC-Fe_3O_4

The apparatus and procedure used for measuring adsorption/desorption were explained in detail in a previously published study [18]. The dynamic adsorption/desorption measurements of the adsorbate (TEX) onto the adsorbent (NC-Fe_3O_4) were performed under atmospheric pressure. The adsorbate flow through the adsorption column was ensured by keeping the inlet concentration values (C_{in}, mg L^{-1}) at constant levels in the adsorption experiments. For adsorption in a single-component system, fixed-bed saturation was attained when the concentration values at the outlet of the adsorption column reached inlet concentration values. For adsorption in the multicomponent systems, on the other hand, fixed-bed saturation was achieved when the outlet concentration (C_{out}, mg L^{-1}) value of each component reached inlet concentration values. A gas chromatography (GC) device (Buck Scientific, GC-910) equipped with a flame ionization detector (FID) was employed to measure the inlet and outlet concentrations of each adsorbate during the adsorption processes in the single-component and multicomponent systems. The adsorption experiments in the single-component and multicomponent systems were executed at an adsorption temperature of 25 °C and a feed flow rate (F) of 100 mL min^{-1}, ensuring inlet concentrations of 10, 20, and 30 mg L^{-1} for each component. For each adsorption and desorption test, 100 mg of adsorbent (m) was applied. Desorption (regeneration) experiments were carried out once the adsorption process reached equilibrium. Regeneration process of the adsorbent was achieved at the desorption temperatures (the boiling points) of 110 °C (T), 136 °C (E) and 140 °C (X) for a contact time (t) of 100 min by passing N_2 as the purge gas over the adsorbent placed in an oven. The adsorbent was utilized for 5 consecutive cycles for repeatability tests in adsorption and desorption experiments. The adsorption capacity (q, mg g^{-1}) was calculated by Eq. (1) with the differential between the inlet and outlet concentrations of the adsorbate at equilibrium [19].

$$q = \frac{F}{m}\left(C_{in}t - \int_0^t C_{out}dt\right) \quad (1)$$

3. Results and discussion

3.1. Preparation and characterization of NC-Fe_3O_4

In this study, NC-Fe_3O_4 was prepared with the co-precipitation method to investigate its comparative and competitive adsorption abilities for TEX. The characterization of the synthesized NC-Fe_3O_4 was carried out with the application of different spectroscopic techniques including BET, SEM, EDS, FTIR, and TGA-DTA.

The BET analysis results of the NC-Fe_3O_4 are exhibited in Fig. 1 and textural properties are listed in Table 1. Hysteresis loops were classified according to the criteria of the International Union of Pure and Applied

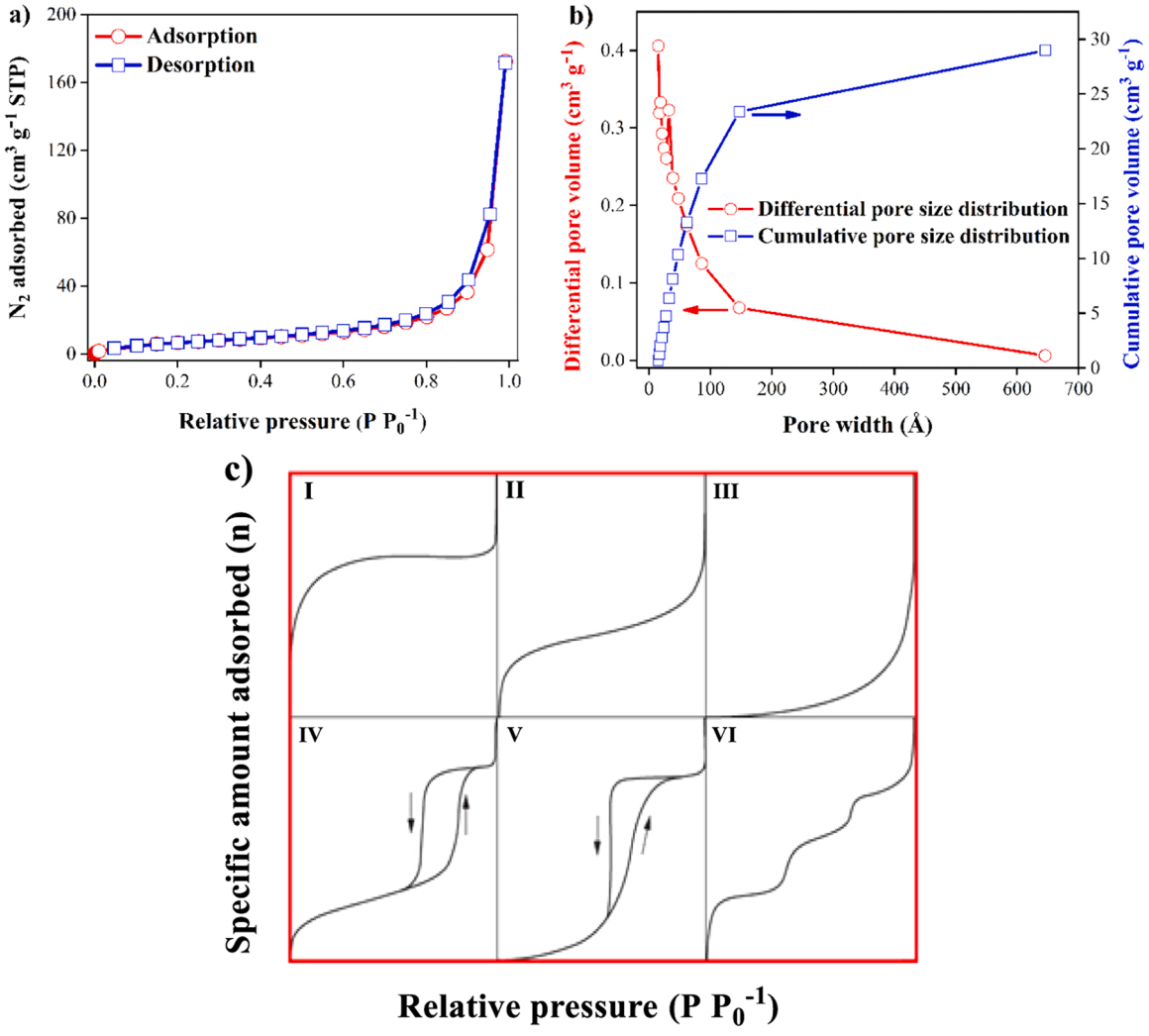

Fig. 1. N_2 adsorption-desorption isotherms at 77 K (a) and pore size distribution (b) for NC-Fe_3O_4, and different types of hysteresis loops of N_2 adsorption at 77 K (c) [20].

Table 1
Textural properties of the NC-Fe_3O_4.

Textural properties	values
Specific surface area ($m^2\ g^{-1}$) (BET)	25.05
Total pore volume ($cm^3\ g^{-1}$)	0.27
Mesopore volume ($cm^3\ g^{-1}$)/fraction (%) (D-R)	0.27/100
Average pore radius (nm)	21.28
Surface area (BJH) ($m^2\ g^{-1}$)	28.96
Pore volume (BJH) ($cm^3\ g^{-1}$)	0.27
Pore radius (BJH) (nm)	8.60
Surface area (DFT) ($m^2\ g^{-1}$)	19.98
Pore volume (DFT) ($cm^3\ g^{-1}$)	0.15
Half pore width (DFT) (nm)	8.01

Chemistry (IUPAC). Evaluation of the hysteresis loops exhibited in Fig. 1c revealed that the NC-Fe_3O_4 has H-3 type hysteresis [20]. Subsequently, the detailed pore textural characteristics of the NC-Fe_3O_4 were determined based on N_2 adsorption-desorption presented in Fig. 1a. The specific surface area of the NC-Fe_3O_4 calculated according to the BET theory was determined to be approximately 25.05 $m^2\ g^{-1}$. Fig. 1b illustrates both differential and cumulative pore size distribution data of the NC-Fe_3O_4. The non-local density functional theory (NLDFT) was employed to elucidate the pore size distribution range. The pore size distribution calculated by means of the Barrett-Joyner-Halenda (BJH) method confirmed that the mean pore diameter was approximately 21.28 nm, indicating pore diameters within the mesoporous range. Furthermore, volume analysis was performed based on the BJH method, and the pore volume of the NC-Fe_3O_4 was determined to be approximately 0.27 $cm^3\ g^{-1}$ [21,22]. When the textural properties of the NC-Fe_3O_4 listed in Table 1 are compared with those of other materials reported in the literature [23], it can be concluded that the specific surface area is lower while the total pore volume and average pore radius are quite high. These are important properties that allow adsorbates to be adsorbed more easily.

Fig. 2a exhibits the SEM image obtained to assess the morphology of the NC-Fe_3O_4. Particles resembling wood logs in Fig. 2a are Fe_3O_4. NC (white or gray according to the angle of light) was observed to cover the Fe_3O_4. The NC-Fe_3O_4 evidently has a smooth and homogeneous surface morphology. The pores and voids are pronounced, and the roughness of the surface indicates the adsorption active sites. The pores, voids, and rough surface provide a significant advantage for increasing the adsorption capacity. In the distribution map in Fig. 2b, the element Fe is observed to be correctly distributed in the NC-Fe_3O_4. In addition, the NC-Fe_3O_4 appears to have both good homogeneity and entrapment. The EDS result presented in Fig. 2b was further used for the characterization of the NC-Fe_3O_4 and strong peaks of Fe, O, and C were observed in the EDS spectrum. The EDS chart exhibits the ratio of the components of the NC-Fe_3O_4 synthesized by means of the co-precipitation method. These outcomes indicate the purity of the synthesis results [24].

The FTIR spectra of the NC-Fe_3O_4 before adsorption and after adsorbing TEX are exhibited in Fig. 3. The FTIR spectra of the NC-Fe_3O_4 before adsorption exhibited in Fig. 3a reveal that the peak of the stretching vibration of the –OH group appeared at 3250 cm^{-1}. The C-H stretching vibration peak appeared at 2910 cm^{-1}. The peak observed at 1620 cm^{-1} was related to the H-O-H bending of the absorbed water. The peak observed at 1400 cm^{-1} was related to the C-H stretching vibration. The peak at 1150 cm^{-1} was related to the C-O antisymmetric stretching. The peak of the bending vibrations of the C-O group appeared at 982 cm^{-1}. The peak recorded at 839 cm^{-1} was due to the bending vibration of the C—H bond. The peak of the bending vibrations of the Fe-O group emerged at 582 cm^{-1}. These recorded peaks are in accordance with the literature [25–28]. According to the FTIR spectra of the NC-Fe_3O_4 after adsorbing TEX exhibited in Fig. 3b, the peak observed in 3662 cm^{-1} belongs to the -OH groups. The peak at 2993 cm^{-1} belongs to the C-H stress peak of the benzene ring. The characteristic peak in 1571 cm^{-1} belongs to the stress-strain C = C in the benzene ring. The

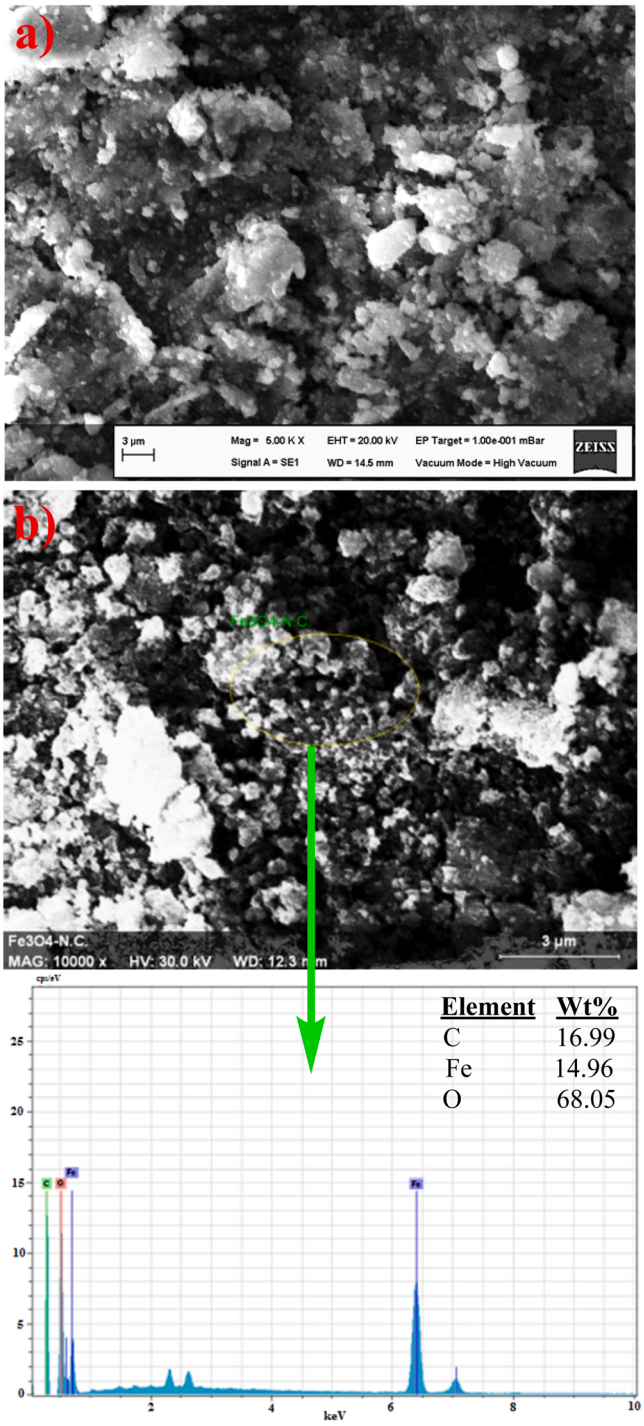

Fig. 2. SEM image (a) and EDS analysis (b) of the NC-Fe_3O_4.

peak at 1480 cm^{-1} is the stretching peak of the C = C bonds in the benzene ring. The peak at about 1391 cm^{-1} is related to the C—H bonds in the benzene ring. These results are compatible with the literature and show that NC-Fe_3O_4 successfully adsorbs TEX [29–31].

The TGA and DTA curves of the NC-Fe_3O_4 before adsorption, and TGA curves of the NC-Fe_3O_4 after adsorbing TEX are presented in Fig. 4. The TGA curves of the NC-Fe_3O_4 reveal the loss of weight to be approximately 39.3% over the temperature range of 25–900 °C. The TGA curves of the NC-Fe_3O_4 can be characterized by two different temperature ranges. Within the range of 25–330 °C, only 15.2% of the weight was lost as a result of residual water loss. Within the range of 330–650 °C, the separation of the cellulose structure and the formation

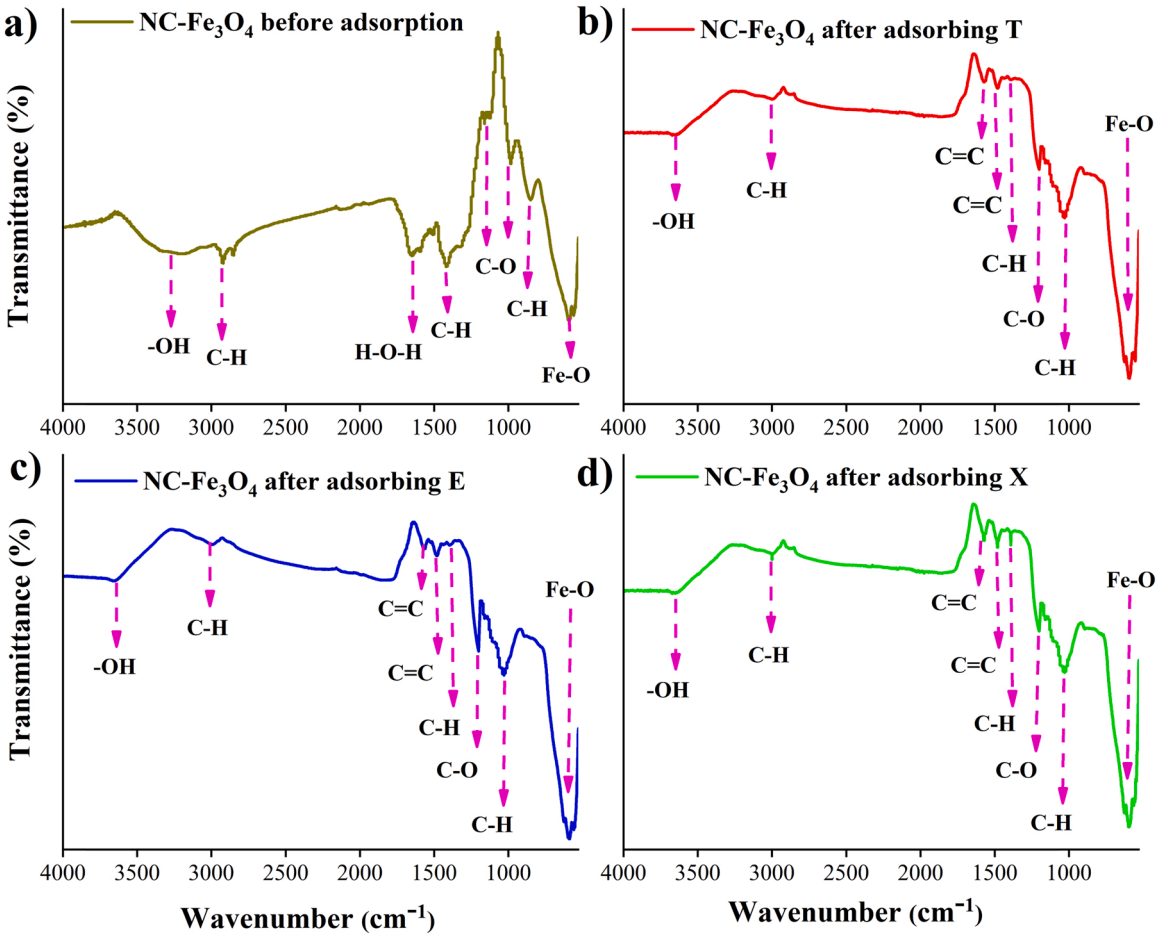

Fig. 3. FTIR spectra of the NC-Fe_3O_4 before adsorption (a) and after adsorbing T (b), E (c), and X (d).

of a vast number of volatiles from the decomposed cellulose units both led to a weight loss of approximately 37.1% as a result of the phase transformation from Fe_3O_4 to Fe-O. The thermal stability of Fe_3O_4 is maintained above 570 °C. The limited reduction in the thermal stability of the NC-Fe_3O_4 did not affect the feasibility of adsorption. According to the TGA curves of the NC-Fe_3O_4 after adsorbing TEX exhibited in Fig. 4b, it can be said that NC-Fe_3O_4 is not adversely affected by desorption (regeneration) temperatures. The stability of the NC-Fe_3O_4 (within the range of 110–140 °C) in the regeneration process can also be understood. Exothermic events were observed in the DTA curve (Fig. 4a). It was surmised that the phase transitions of iron oxide particles occurred consequent to a loss of weight, anticipated to be related to these exothermic events, the combustion of organic matters, and changes in crystal structure [12,32].

3.2. *Comparative and competitive adsorption of TEX onto NC-Fe_3O_4 in single-, binary- and ternary-component systems*

Since VOC pollutants are released in multicomponent systems due to industrial processes, exploring the comparative and competitive adsorption of VOCs is of both practical and scientific interest. Therefore, this study investigated the adsorption behavior of TEX targeted as VOCs in both single-component and multicomponent mixtures onto the NC-Fe_3O_4.

The adsorption capacities of TEX onto the NC-Fe_3O_4 in single-, binary- and ternary-component systems were studied at various TEX inlet concentrations (10, 20, and 30 mg L^{-1}) and the results are presented in Figs. 5–8, and 9, respectively.

As revealed in Fig. 5, which presents the results for the single-component system, the approximate adsorption capacities at 10, 20, and 30 mg L^{-1} TEX inlet concentrations were determined as 343, 477, and 485 mg g^{-1} for T; as 415, 550, and 563 mg g^{-1} for E; and as 462, 578, and 595 mg g^{-1} for X, respectively.

Fig. 6, presenting the results for T-E and T-X in the binary-system, reveals that the adsorption capacity for T at T inlet concentrations of 10, 20, and 30 mg L^{-1} was decreased in comparison to the single-component system by approximately 60% and 71% for 10 mg L^{-1} T + 10 mg L^{-1} E and 10 mg L^{-1} T + 10 mg L^{-1} X, respectively; by 43% and 50% for 20 mg L^{-1} T + 10 mg L^{-1} E and 20 mg L^{-1} T + 10 mg L^{-1} X, respectively; and by 41% and 47% for 30 mg L^{-1} T + 10 mg L^{-1} E and 30 mg L^{-1} E + 10 mg L^{-1} X, respectively. This decrease in the adsorption capacity of T is evidence of the competitive dominance of the E and X over the T for adsorption sites [33].

Similarly, it is observed in Fig. 7, which presents the results for E-T and E-X in the binary-component system, that the adsorption capacity for E at E inlet concentrations of 10, 20, and 30 mg L^{-1} was decreased in comparison to the single-component system by approximately 36% and 60% for 10 mg L^{-1} E + 10 mg L^{-1} T and 10 mg L^{-1} E + 10 mg L^{-1} X, respectively; by 27% and 46% for 20 mg L^{-1} E + 10 mg L^{-1} T and 20 mg L^{-1} E + 10 mg L^{-1} X, respectively; and by 26% and 44% for 30 mg L^{-1} E + 10 mg L^{-1} T and 30 mg L^{-1} E + 10 mg L^{-1} X, respectively. For the E-T mixture, the considerably low decrease observed in the adsorption capacity of E was a manifestation of the competitive dominance of the E over the T for adsorption sites. On the other hand, in the binary-mixture of E-X, the significant decrease in the adsorption capacity of E indicates competitive dominance of the X over the E for adsorption sites [34].

Furthermore, with the results for X-T and X-E in the binary-

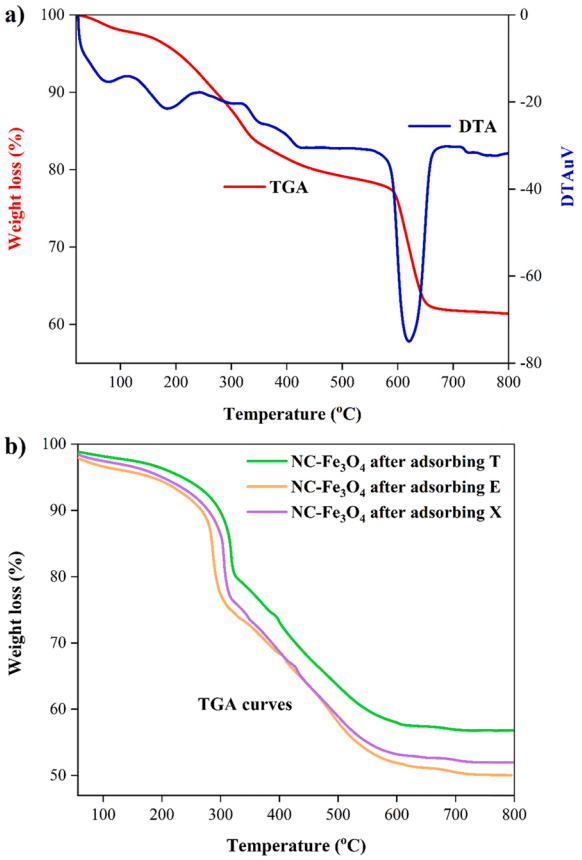

Fig. 4. TGA and DTA curves of the NC-Fe_3O_4 before adsorption (a), and TGA curves of the NC-Fe_3O_4 after adsorbing TEX (b).

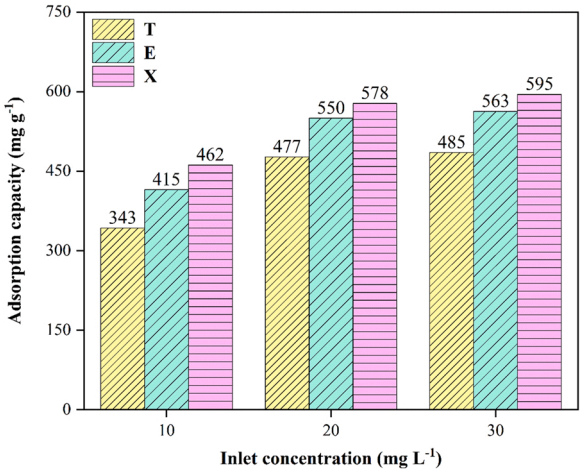

Fig. 5. Comparative adsorption capacities of TEX onto NC-Fe_3O_4 in a single-component system.

component system exhibited in Fig. 8, it was observed that the adsorption capacity for X at X inlet concentrations of 10, 20, and 30 mg L^{-1} was decreased in comparison to the single-component system by approximately 19% and 27% for 10 mg L^{-1} X + 10 mg L^{-1} T and 10 mg L^{-1} X + 10 mg L^{-1} E, respectively; by 16% and from 21% for 20 mg L^{-1} X + 10 mg L^{-1} T and 20 mg L^{-1} X + 10 mg L^{-1} E, respectively; and by 15% and 20% for 30 mg L^{-1} X + 10 mg L^{-1} T and 30 mg L^{-1} X + 10 mg L^{-1} E, respectively. In the mixtures of both X-T and X-E, the adsorption capacity of X remained consistent with a negligible decrease, which can be ascribed to the competitive dominance of the X over the T

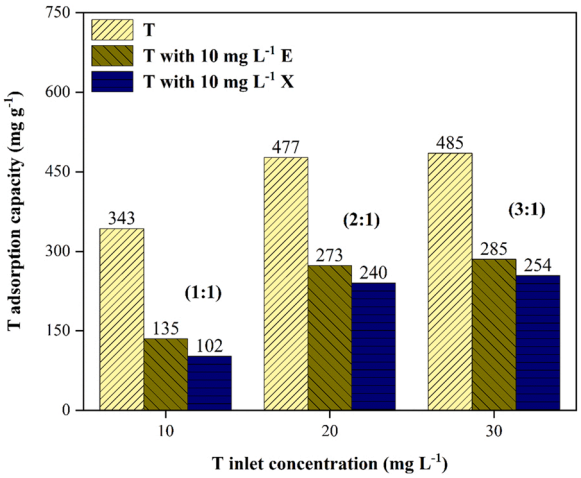

Fig. 6. Competitive adsorption capacity of T onto NC-Fe_3O_4 in a binary-component system.

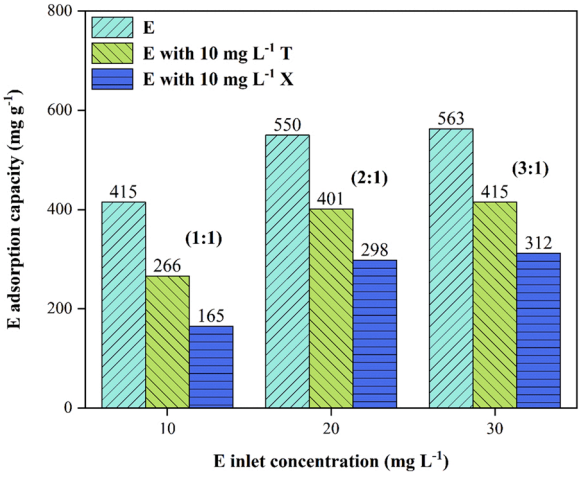

Fig. 7. Competitive adsorption capacity of E onto NC-Fe_3O_4 in a binary-component system.

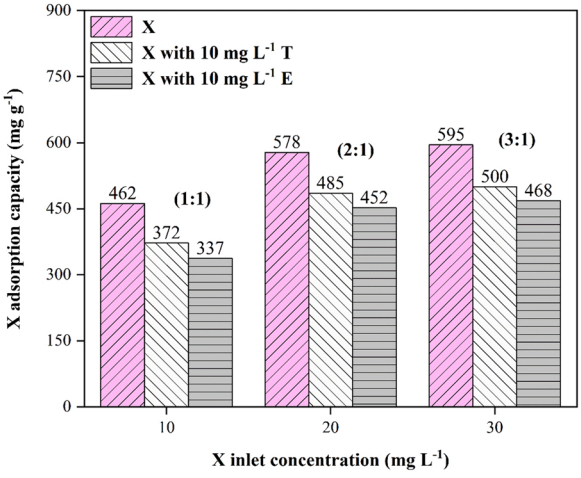

Fig. 8. Competitive adsorption capacity of X onto NC-Fe_3O_4 in a binary-component system.

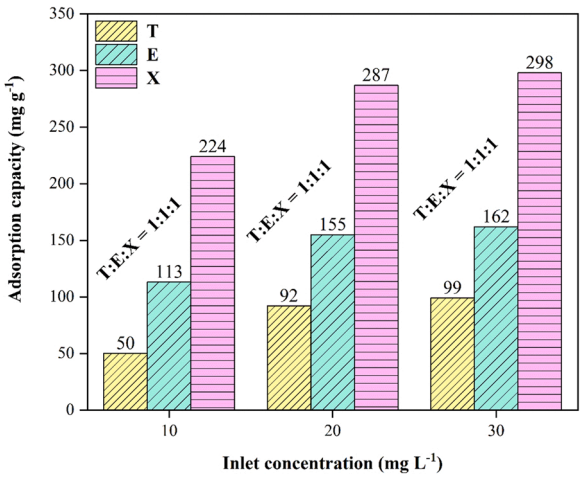

Fig. 9. Competitive adsorption capacities of TEX onto NC-Fe_3O_4 in a ternary-component system.

and E for adsorption sites [34].

In Fig. 9, which demonstrates the TEX results for the ternary-component system, the adsorption capacities of TEX were determined as 50, 113, and 224 mg g^{-1}, respectively, for the 10 mg L^{-1} mixture of TEX (T:E:X = 1:1:1); as 92, 155, and 287 mg g^{-1}, respectively, for the 20 mg L^{-1} mixture of TEX (T:E:X = 1:1:1); and as 99, 162, and 298 mg g^{-1}, respectively, for the 30 mg L^{-1} mixture of TEX (T:E:X = 1:1:1). The competitive adsorption capacities acquired in the ternary-component system were observed to be lower compared to the outcomes obtained for the single-component system (Fig. 5). In this process, once TEX as a ternary-component has reached the surface of the adsorbent, the most strongly adsorbed X is preferentially retained on the adsorbent and displaces the weakly adsorbed E, while E retains a position on the adsorbent by replacing the most weakly adsorbed T. Consequently, the adsorption ability of the NC-Fe_3O_4 followed the order of X > E > T in the ternary-component system, in agreement with the adsorption observed for the single-component system. These findings provide strong support for a better understanding of the comparative and competitive adsorption behaviors among different gaseous VOC pollutants in relation to a particular adsorbent.

Compared to the single-component system, the TEX exhibited divergent competitive adsorption capacities at varying inlet concentrations in the binary- and ternary-component systems. The adsorption capacity of each component in a multicomponent system was remarkably lower compared to that in the single-component system. Furthermore, the adsorption capacity of the X in multicomponent systems was greater compared to both the T and E. These results indicate that the adsorption selectivity of the NC-Fe_3O_4 for X is higher than that for E and T. Moreover, the order of X > E > T observed for adsorption capacities in single-, binary-, and ternary-component systems can be explained by the different molecular weights, methyl groups, and physical adsorption binding energies of the T, E, and X [35,36].

3.3. Elucidation of comparative and competitive adsorption mechanisms of TEX onto NC-Fe_3O_4

Considering the large volume, abundance, and size (width, thickness, and length) of the pores, it was easy to access the pores of the adsorbent due to the small molecular dimensions of the TEX. Adsorption is related to activation/modification methods and can be controlled by physical and chemical processes. The chemical functional groups of the surface of an adsorbent are responsible for the abilities and behaviors of the adsorption. The present surface functional groups govern the surface chemistry. These groups contribute to the bonding of TEX to the surface of the adsorbent based on the affinity between adsorbate and surface functional groups [27]. Despite the low specific surface area of the synthesized adsorbent, the high TEX adsorption capacity can be associated with the adsorbent-adsorbate relationship, as well as the physical and chemical properties of the adsorbent, depending on the nature of the adsorbed TEX [37,38].

Although we cannot hypothesize a precise mechanism for the competitive adsorption process, it is known that a multitude of factors take part in the mechanism. In the ternary-mixture of TEX, the physical properties, chemical properties, affinity, dipole moment (X > E > T), boiling point (X > E > T), and molecular weight (X = E > T) of each gas are essential factors in the relevant competitive adsorption mechanism. Intermolecular attraction (van der Waals force), specific surface area, pore structure, and pore volume determine the physical properties of the adsorbent. Physical adsorption is a reversible process. The functional groups contained within the adsorbent surface determine the chemical properties of the adsorbent. In the adsorption process, physical adsorption and chemical adsorption can occur simultaneously. A gas with high affinity occupies more space in the adsorbent area than a gas with low affinity. A gas with a higher boiling point and higher molecular weight exhibits greater adsorption affinity. X has two methyl groups while E has one ethyl group and T has one methyl group. The methyl group is electron-donating. It provides electron abundance to the ring. Electron-donating groups have a positive inductive effect (X > E > T). They activate the rings and make them more reactive. The π-electrons in the rings are assumed to be exhibiting π-π interactions with the NC-Fe_3O_4 regions that are rich in π-electrons. However, hydrogen bonds may have formed between the hydrogens in the rings and the oxygens in the NC-Fe_3O_4. Since hydrogen density will increase as methyl groups increase in a ring, a ring with more methyl groups develops more hydrogen bonds (X > E > T). An electrostatic interaction (X > E > T) due to electron clouds is also assumed to be occurring during the interaction between NC-Fe_3O_4 and TEX [37,38].

3.4. Comparison of the adsorption capacity of Fe_3O_4 and NC-Fe_3O_4 with other reported materials for the removal of TEX

Considering the results listed in Table 2, it is clear that there is a significant increase in the adsorption capacity of the NC-F_3O_4 compared to Fe_3O_4. It can also be observed that the NC-F_3O_4 has significant

Table 2
Comparison of the adsorption capacity of Fe_3O_4 and NC-Fe_3O_4 with other reported materials in the literature for the removal of TEX.

Adsorbate	Adsorbent	Adsorption capacity (mg g^{-1})	Reference
T	Biochar	65.50	[39]
	Granular activated carbon	118.00	[40]
	Rice husk char	263.60	[41]
	CTAB-U-0.5	275.00	[42]
	rGO	304.40	[43]
	Silica gel	353.82	[44]
	Cu-BTC@GO	460.70	[45]
	Fe_3O_4	354.80	This work
	NC-Fe_3O_4	485.35	This work
E	MOF-5	99.00	[46]
	Zn(BDC)-$(Dabco)_{0.5}$	347.00	[47]
	PCH	451.21	[48]
	MIL-101	1105.00	[49]
	Fe_3O_4	423.95	This work
	NC-Fe_3O_4	563.17	This work
X	Bentonite	110.62	[50]
	Granular activated carbon	139.00	[40]
	Zn(BDC)-$(Dabco)_{0.5}$	342.00	[47]
	Activated carbon	588.23	[21]
	HN-PC	594.50	[51]
	Fe_3O_4	451.57	This work
	NC-Fe_3O_4	595.12	This work

potential in the removal of TEX compared to other reported materials in the literature (Table 2). All these results confirm that the modification of F_3O_4 with NC is a highly effective strategy.

3.5. Adsorption kinetic models of TEX onto NC-Fe_3O_4

The adsorption mechanism of TEX onto the NC-Fe_3O_4 was elucidated by fitting the reaction-based (quasi-first-order (Q-FO) model and quasi-second-order (Q-SO) model) and diffusion-based rate-limiting (intra-particle diffusion model, Boyd's film-diffusion model, and mass transfer model) kinetic models to the experimental adsorption data. It is imperative to estimate the kinetics of an ongoing adsorption process when attempting to implement an effective adsorption process. A number of kinetic models have been studied to date for this purpose. Among the kinetic models proposed in the literature, reaction-based Q-FO and Q-SO kinetic models, which provide simpler descriptions for adsorption kinetics and adsorbent-adsorbate interaction, are common [52,53]. The Q-FO kinetic model assumes the absence of pollutant (adsorbate) ions on the adsorbent surface in the beginning, while the adsorbate is presumed to occupy the adsorbent surface as time progresses. The Q-SO kinetic model, on the other hand, is based on the adsorption equilibrium capacity of the adsorption system. It assumes that the adsorption capacity of the adsorbent is related to the number of non-utilizable sites on the surface [54]. The nonlinear forms of the reaction-based Q-FO and Q-SO kinetic models are presented by Eqs. (2) and (3), respectively.

$$q_t = q_e(1 - e^{-k_1 \quad t}) \tag{2}$$

$$q_t = \frac{k_2 \quad q_e^{\,2} \quad t}{1 + k_2 \quad q_e \quad t} \tag{3}$$

In these equations, the adsorption capacity at equilibrium, the adsorption capacity at time t (min), the rate constant of the Q-FO kinetic model, and the rate constant of the Q-SO kinetic model are described by q_e (mg g^{-1}), q_t (mg g^{-1}), k_1 (min^{-1}), and k_2 (g min^{-1} mg^{-1}), respectively [13,55].

The validity of the fittings of the kinetic models was assessed using the statistics of root mean square error (*RMSE*) and mean absolute error (*MAE*) [56]:

Reaction-based kinetic models employed to predict the adsorption behavior of adsorbents are insufficient to provide a profound understanding of the process mechanism controlling the adsorption kinetics [57]. Therefore, diffusion-based rate-limiting kinetic models such as the intra-particle diffusion model, Boyd's film-diffusion model, and the mass transfer model were applied to elucidate the process mechanism in the adsorption of TEX onto NC-Fe_3O_4. Representative formulations of these models are given in Eqs. (4), (5–7), and (8–11):

$$q_t = k_{id} \quad t^{0.5} + C \tag{4}$$

$$B_t = -0.4977 - ln(1 - F) \rightarrow (\mathrm{F} > 0.85) \tag{5}$$

$$B_t = (\sqrt{\pi} - \sqrt{\pi - \left(\frac{\pi^2 \quad F}{3}\right)})^2 \rightarrow (\mathrm{F} < 0.85) \tag{6}$$

$$F = \frac{q_t}{q_e} \tag{7}$$

$$q_t = B + \frac{1}{\beta} ln(t) \tag{8}$$

$$B = \frac{ln \quad [k_L a]_g - ln \quad \left\{ ln \quad \frac{C_0}{C_t} \right\}}{\beta} \tag{9}$$

$$[k_L a]_f = [k_L a]_g \times e^{-\beta \quad ln \quad (Q_t)} \tag{10}$$

$$[k_L a]_d = [k_L a]_g - [k_L a]_f \tag{11}$$

In these equations, k_{id} (mg g^{-1} $min^{-1/2}$), C, F, B_t (nondimensional), B (mg g^{-1}), β (g min^{-1} mg^{-1}), $[k_L a]_g$ (min^{-1}), $[k_L a]_f$ (min^{-1}), and $[k_L a]_d$ (min^{-1}) represent the intraparticle diffusion rate constant, the intersection point related to the boundary layer thickness, the fractional adsorption capacity at a certain time, a mathematical function of F, the potential mass transfer index related to the driving force of mass transfer, the adsorbate-adsorbent affinity parameter, the general mass transfer factor, the film mass transfer factor or external mass transfer factor, and the porous diffusion factor or internal mass transfer factor, respectively [12].

For the kinetic evaluation of the adsorption process of TEX onto NC-Fe_3O_4, the reaction- and diffusion-based kinetic models were fitted to the experimental data acquired under the conditions of 20 mg L^{-1} TEX inlet concentrations, adsorption temperature of 25 °C, and different contact times (10, 20, 30, 40, 50, 60, 70, 80, 90, and 100 min). Fig. 10 exhibits the plot fitted for the reaction-based Q-FO and Q-SO kinetic models. A summary of the kinetic model constants and fitting data calculated by the least-squares regression is provided in Table 3. Within the framework of the data presented in Table 3 and Fig. 10, the R^2 values of the Q-FO kinetic model are higher than those of the Q-SO kinetic model and the calculated equilibrium adsorption capacity values are also closer to the experimental outcomes. In addition, the accuracy analysis of the Q-FO and Q-SO kinetic models was evaluated with *RMSE* and *MAE* statistics. Compared to the Q-SO kinetic model, the low *RMSE* (8.13, 8.26, and 7.59 for T, E, and X, respectively) and *MAE* (6.76, 6.79, and 5.85 for T, E, and X, respectively) values of the Q-FO kinetic model confirm that it is more consistent with the experimental results (Table 3). These findings thus indicate that the adsorption process of TEX is better described by means of the Q-FO kinetic model. Furthermore, the adsorption processes of TEX onto NC-Fe_3O_4, which follow the Q-FO kinetic model, reveal the physical adsorption mechanism [58].

The fact that the intra-particle diffusion model yields a linear line passing through the starting point of the plot indicates that the model in question has a rate-limiting step. The nonlinear plot of q_t against $t^{1/2}$, exhibited in Fig. 11a, indicates that other rate-limiting steps also have effects on the adsorption process, apart from the intra-particle diffusion resistance. The curves acquired for the adsorption of TEX onto NC-Fe_3O_4 exhibited three linear steps. This finding can be attributed to the mechanisms involving three steps. The adsorption process starts with the diffusion step of the TEX to the outer surface of the adsorbent (i), followed by the gradual adsorption of the TEX against the inner zones defined as macropores, mesopores, and micropores (ii) and completed with the final step of equilibrium of intraparticle diffusion (iii) [59,60].

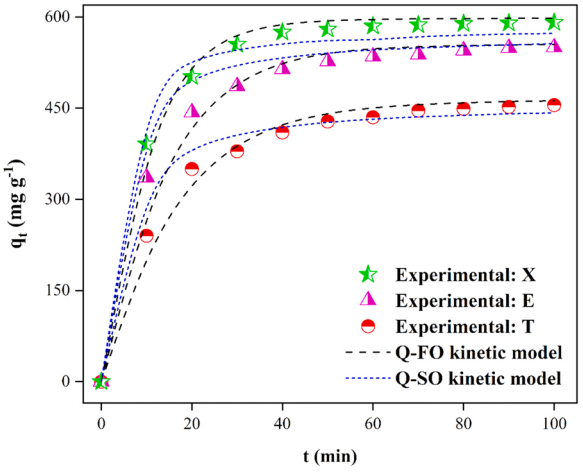

Fig. 10. Reaction-based kinetic models fitted for the adsorption of TEX onto NC-Fe_3O_4.

Table 3
Summary of nonlinear reaction- and diffusion-based kinetic model constants and their fitting data for the adsorption of TEX onto NC-Fe_3O_4.

Kinetic models	Parameters	T	E	X
Reaction-based models				
Q-FO model	q_e (mg g^{-1})	462.53	555.08	597.55
	k_1 (min^{-1})	0.06	0.07	0.11
	R^2	0.997	0.996	0.999
	RMSE	8.13	8.26	7.59
	MAE	6.76	6.79	5.85
Q-SO model	q_e	459.77	572.08	585.48
	k_2 (g min^{-1} mg^{-1})	5.71 × 10^{-4}	6.09 × 10^{-4}	8.25 × 10^{-4}
	R^2	0.972	0.981	0.980
	RMSE	28.97	27.53	27.60
	MAE	17.29	19.92	20.25
Diffusion-based models				
Intra-particle diffusion model	k_{id} (mg g^{-1} $min^{-1/2}$)	36.50	41.77	44.48
	C	121.79	165.56	206.30
Mass transfer model	*B* (mg g^{-1})	102.10	185.07	268.32
	B (g min^{-1} mg^{-1})	0.010	0.011	0.013

Boyd's film-diffusion model was also applied to confirm the findings of the intra-particle diffusion model. Boyd's film-diffusion model is based on the external mass transfer resistance of a gas film on an adsorbent surface as the main resistance to the adsorption process and also considers whether this resistance is a rate-limiting step. A line passing through the origin of the plot obtained based on Boyd's film-diffusion model confirms that the mass transfer rate is controlled by intraparticle diffusion. Otherwise, it is assumed that the rate of adsorption is also controlled by the film-diffusion mechanism [57]. Nonlinear illustrations of B_t against time (t) obtained for Boyd's film-diffusion model, provided in Fig. 11b, revealed that intraparticle diffusion was not the only factor affecting the adsorption process. In other words, these findings, which are compatible with the nonlinear graph of the intraparticle diffusion model, indicate that multiple processes affect the adsorption of TEX. Therefore, taken together, these evaluations demonstrate that the adsorption processes of TEX onto the NC-Fe_3O_4 are affected by both film-diffusion resistance (first stage) and intra-particle diffusion resistance (after the TEX molecules diffuse through the gas film).

The mass transfer model was fitted to fully elucidate the dynamic adsorption behavior of TEX onto the NC-Fe_3O_4. Extensive investigation of the adsorption mechanism and thus determination of the most effective mass transfer factor are suggested to be related to mass transfer resistance. Mass transfer resistance can be affected by either film diffusion or porous diffusion, or both. The mass transfer resistance affected by the porosity of the applied adsorbent can control the adsorption capacity to a considerable extent [61,62]. In order to evaluate these possible behaviors, the general mass transfer factor of the mass transfer model ($[k_La]_g$), external (film) mass transfer factor ($[k_La]_f$), and internal diffusion factor ($[k_La]_d$) were determined. Against the C_t/C_0 (%) acquired for this model, the plots of change of $[k_La]_g$, $[k_La]_f$, and $[k_La]_d$ are exhibited in Figs. 11c, 11d, and 11e, respectively. At this point, by increasing the C_t/C_0 (%) values, the rates of factors $[k_La]_g$, $[k_La]_f$, and $[k_La]_d$ were observed to decrease based on adsorption. Based on the values of the mass transfer factors determined for the adsorption of TEX onto NC-Fe_3O_4, the order of mass transfer diffusion rate was T < E < X. On the other hand, the general mass transfer and film mass transfer factors calculated for the adsorption of TEX were found to be higher than the internal diffusion factors ($[k_La]_g > [k_La]_f > [k_La]_d$). The fact that the values for general mass transfer and film mass transfer were higher than values for internal diffusion reveals the physical adsorption mechanism.

3.6. Adsorption isotherm models of TEX onto NC-Fe_3O_4

Langmuir, Freundlich, and Dubinin-Radushkevich (D-R) isotherm models were applied to describe the adsorption equilibrium mechanism regarding the adsorption of TEX onto the NC-Fe_3O_4. The Langmuir isotherm model assumes that adsorption occurs on a monolayer surface containing a limited number of adsorption sites of the adsorbent and that no further adsorption takes place on this surface. The maximum adsorption of the surface can be achieved when the surface reaches saturation. This translates into adsorption sites that are energy-equivalent monotype constructs, and the maximum adsorption is attained when the surface reaches saturation. The Freundlich isotherm describes the adsorption type on a heterogeneous surface in interaction with adsorbed molecules. The adsorption energy assumes an exponential decrease in the polymer with respect to the adsorption center and the reversible adsorption is thus completed and is not limited to the formation of a single layer [63]. The D-R isotherm is an empirical model designed to reflect the adsorption of subcritical vapors on microporous solids subsequent to an initial pore-filling mechanism. It is generally applied to describe the mechanism of adsorption with Gaussian energy distribution on heterogeneous surfaces. The approach is usually employed to distinguish between physical and chemical adsorption [64]. The nonlinear forms of the applied isotherm models are provided in Eqs. (12,13), and (14–16), respectively:

$$q_e = \frac{q_m \quad K_L \quad C_e}{1 + \quad K_L \quad C_e} \tag{12}$$

$$q_e = K_f \quad C_e^{\frac{1}{n}} \tag{13}$$

$$q_e = q_s exp\left(-\beta\varepsilon^2\right) \tag{14}$$

$$\varepsilon = RTln\left(1 + \frac{1}{C_e}\right) \tag{15}$$

$$E = \frac{1}{\sqrt{2\beta}} \tag{16}$$

In these equations, K_L (L mg^{-1}), C_e (mg L^{-1}), q_m (mg g^{-1}), q_e (mg g^{-1}), K_f (mg g^{-1})(L mg^{-1})$^{1/n}$, n, q_s (mg g^{-1}), β (mol^2 kJ^{-2}), ε (J mol^{-1}), R (kJ mol^{-1} K^{-1}), T (K), and E (kJ mol^{-1}) describe the Langmuir model constant, equilibrium concentration of TEX, maximum single-layer adsorption capacity, adsorption capacity at equilibrium, Freundlich model constant, Freundlich model constant related to adsorption density, maximum adsorption capacity, activity coefficient constant related to adsorption energy, Polanyi adsorption potential, ideal gas constant, absolute temperature, and mean free adsorption energy, respectively [62].

The validity of the fittings of the isotherm models was assessed with *RMSE* and *MAE* statistics. To evaluate the equilibrium mechanism of the adsorption process of TEX onto NC-Fe_3O_4, the isotherm models were fitted to the experimental data acquired under the conditions of 100 min of contact time, adsorption temperature of 25 °C, and varying TEX inlet concentrations (5, 10, 15, 20, 25, 30, and 35 mg L^{-1}). Fig. 12 exhibits a representative fitted plot of the isotherm models. A summary of the isotherm model constants and fitting data calculated by least-squares regression is provided in Table 4. Based on the data in Table 4 and Fig. 12, the D-R model describes the experimental data more effectively than the other models. Accuracy analysis of the Langmuir, Freundlich, and D-R isotherm models was also performed using *RMSE* and *MAE*. Compared to the other models, the low *RMSE* (6.33, 7.40, and 7.58 for T, E, and X, respectively) and *MAE* (5.12, 5.25, and 5.75 for T, E, and X, respectively) values confirm that the D-R model better fits the obtained experimental results (Table 4). In this study, the n values (Freundlich model constant) were calculated as 1.85, 3.52, and 4.00 for T, E, and X, respectively, indicating an efficient adsorption process [65]. In addition, n values greater than 1 indicate a physical adsorption process [66].

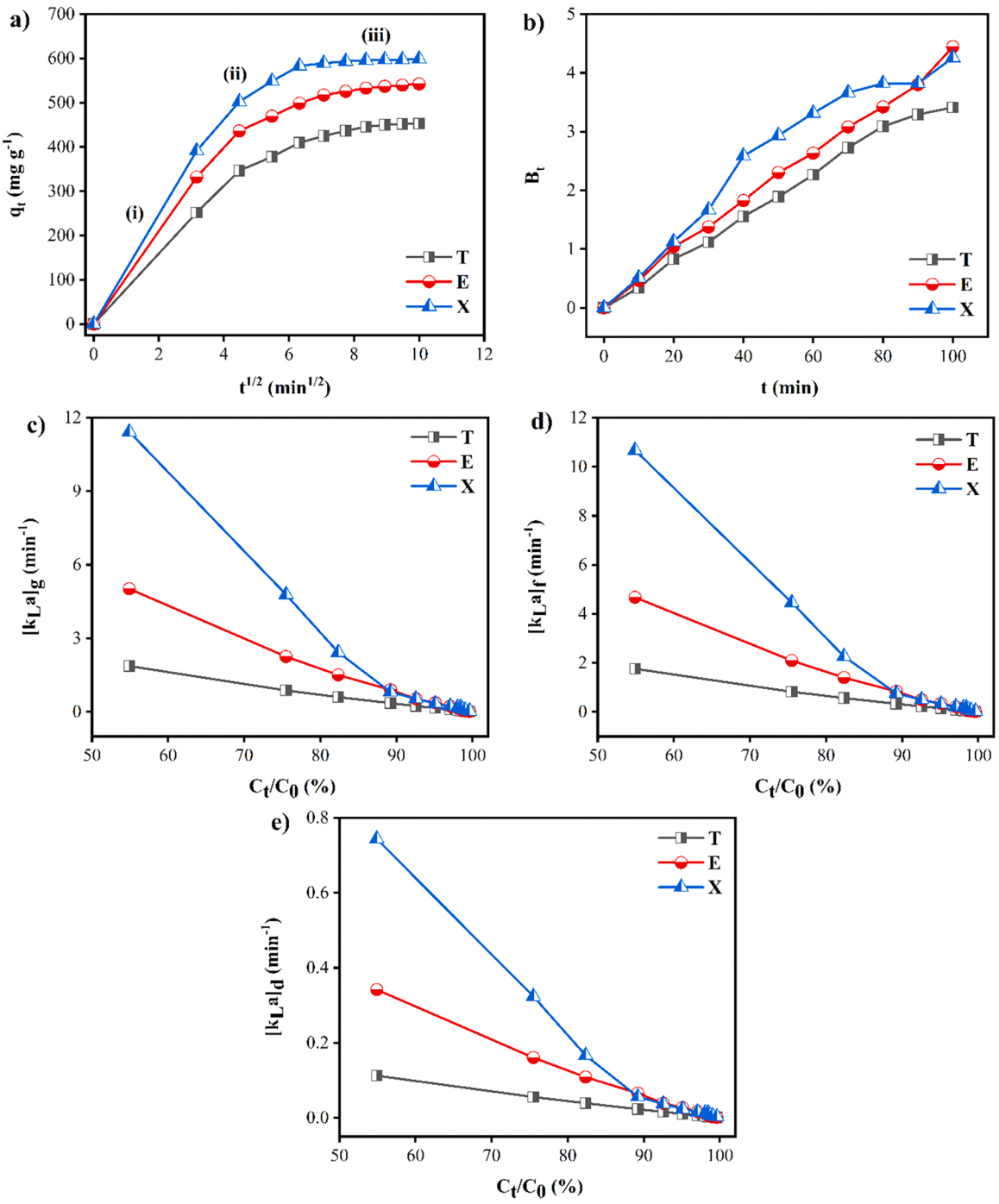

Fig. 11. Diffusion-based intra-particle diffusion model (a), Boyd's film-diffusion model (b), $[k_L a]_g$ (general mass transfer factor) (c), $[k_L a]_f$ (film mass transfer factor) (d), $[k_L a]_d$ (porous diffusion factor or internal mass transfer factor), and (e) mass transfer factors' variation for the adsorption of TEX onto NC-Fe_3O_4.

Moreover, the *E* values (D-R model constant) were calculated as 1.55, 2.22, and 2.33 kJ mol^{-1} for T, E, and X, respectively, indicating that the adsorption process takes place through a mechanism of physical interaction [62].

3.7. Regeneration and reusability of NC-Fe_3O_4

In evaluating the applicability of any method developed for adsorbents, regeneration and reuse efficiency are very important considerations. In addition, the reusability of the developed adsorbents is an important criterion in terms of practical applications and the cost of the adsorption process. Fig. 13 presents the reuse efficiency results provided by five consecutive adsorption-desorption cycle tests of the NC-Fe_3O_4 conducted with gaseous TEX. The findings in Fig. 13 reveal that the NC-Fe_3O_4 sustains a reuse efficiency of 92.50%, 90.15%, and 89.84% for T, E, and X, respectively. The high regeneration and reuse efficiency achieved in this study indicate that the interactions between the NC-Fe_3O_4 and TEX were possibly van der Waals force orπ-π interactions [55,67]. On the other hand, the formation of permanent bonds on the adsorbing surface and the irreversible transformation of the adsorbed groups may have originated from incomplete desorption/regeneration processes. In other words, it is probable that some chemically bound adsorbates that are not desorbed may clog the pores and thus cause residue formation [68].

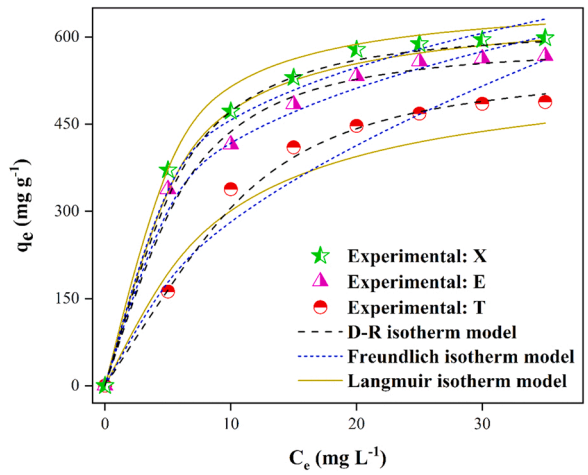

Fig. 12. Isotherm models fitted for the adsorption of TEX onto NC-Fe_3O_4.

Table 4
Summary of nonlinear Langmuir, Freundlich, and D-R isotherm model constants and their fitting data for the adsorption of TEX onto NC-Fe_3O_4.

Isotherm models	Parameters	T	E	X
Langmuir	q_{max} (mg g^{-1})	555.56	656.60	672.95
	K_L (L mg^{-1})	0.12	0.27	0.35
	R^2	0.975	0.986	0.985
	RMSE	19.31	17.83	14.08
	MAE	16.63	14.75	11.87
Fruendlich	K_F [(mg g^{-1}) (L mg^{-1})$^{1/n}$]	81.94	218.98	259.30
	n	1.85	3.52	4.00
	R^2	0.983	0.988	0.989
	RMSE	11.74	20.61	28.61
	MAE	10.08	16.63	26.25
D-R	q_s (mg g^{-1})	544.03	583.16	615.00
	β (mol^2 kJ^{-2})	2.07×10^{-5}	1.01×10^{-5}	0.92×10^{-5}
	E (kJ mol^{-1})	1.55	2.22	2.33
	R^2	0.998	0.996	0.998
	RMSE	6.33	7.40	7.58
	MAE	5.12	5.25	5.75

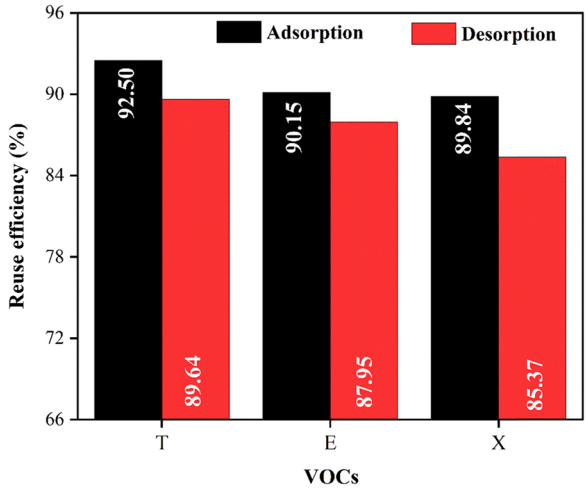

Fig. 13. Reuse efficiency of NC-Fe_3O_4 for TEX after five consecutive adsorption/desorption cycles.

4. Conclusions

This study has elucidated the adsorption behavior of TEX targeted as VOCs onto NC-Fe_3O_4 both individually and in multicomponent systems. Characterization of the NC-Fe_3O_4 synthesized with the co-precipitation method was carried out by some analysis techniques including FTIR, BET, SEM, EDS, and TGA-DTA. The adsorption capacities of T, E, and X as single-components onto the NC-Fe_3O_4 for 20 mg L^{-1} TEX inlet concentrations were found to be 477, 550, and 578 mg g^{-1}, respectively. In contrast, with TEX in a two-component system, the adsorption capacity of the T (for 20 mg L^{-1} T with 10 mg L^{-1} E and 10 mg L^{-1} X, respectively) decreased by approximately 43% and 50% for the binary-mixtures of T-E and T-X, respectively, due to competition with E and X for adsorption sites. Similarly, the adsorption capacity of the E (for 20 mg L^{-1} E with 10 mg L^{-1} X) decreased by approximately 46% due to competition with X for adsorption sites. With TEX in a ternary-component system, the adsorption capacity of the X remained consistent, indicating its competitive dominance over E and T. The adsorption capacity of the NC-Fe_3O_4 followed the order of X > E > T in the ternary-component system, which agrees with the adsorption seen in the single-component system. In the ternary-mixture of TEX, each gas has its own physical properties, chemical properties, affinity, dipole moment (X > E > T), boiling point (X > E > T), and molecular weight (X = E > T), which are important factors for the competitive adsorption mechanism. The adsorption of TEX was explained by fitting the adsorption data to diverse kinetic and isotherm models. The adsorption processes of TEX on the NC-Fe_3O_4 following the Q-FO kinetic and D-R isotherm models indicated the physical adsorption mechanism. Moreover, based on the evaluations of the applied diffusion-based intra-particle diffusion and Boyd's film-diffusion kinetic models, it was concluded that the adsorption processes of TEX are affected by both film-diffusion resistance (first step) and intra-particle diffusion resistance (after the TEX molecules diffuse through the gas film). Based on the values of the mass transfer factors, it was observed that the order of mass transfer diffusion rate was T < E < X. On the other hand, the general mass transfer and film mass transfer factors were found to be higher than the internal diffusion factor. The fact that the general mass transfer and film mass transfer were higher than internal diffusion supports the physical adsorption mechanism. The high regeneration and reuse efficiency obtained in this study further indicate that interactions between the NC-Fe_3O_4 and TEX are possibly van der Waals force or π-π interactions. The reuse efficiency of the innovative adsorbent after 5 cycles was higher than 89%. Therefore, NC-Fe_3O_4 may be used as a promising and renewable adsorbent for the efficient treatment of VOC pollutants. These findings will be helpful for acquiring a better understanding of the comparative and competitive adsorption behaviors between different VOC pollutants in relation to a given adsorbent.

CRediT authorship contribution statement

Mehmet Şakir Ece: Conceptualization, Writing – review & editing.
Sinan Kutluay: Conceptualization, Writing – review & editing.

Declaration of Competing Interest

The authors declare that they have no known competing financial interests or personal relationships that could have appeared to influence the work reported in this paper.

References

[1] R.K. Ibrahim, M. Hayyan, M.A. AlSaadi, A. Hayyan, S. Ibrahim, Environmental application of nanotechnology: air, soil, and water, Environ. Sci. Pollut. Res. 23 (2016) 13754–13788.
[2] M. Shafiei, M.S. Alivand, A. Rashidi, A. Samimi, D. Mohebbi-Kalhori, Synthesis and adsorption performance of a modified micro-mesoporous MIL-101 (Cr) for VOCs removal at ambient conditions, Chem. Eng. J. 341 (2018) 164–174.

[3] E. Batur, O. Baytar, S. Kutluay, S. Horoz, Ö. Şahin, A comprehensive new study on the removal of Pb (II) from aqueous solution by şırnak coal-derived char, Environ. Technol. 42 (2021) 505–520.
[4] M.Ş. Ece, S. Kutluay, Ö. Şahin, Silica-coated magnetic Fe3O4 nanoparticles as efficient nano-adsorbents for the improvement of the vapor-phase adsorption of benzene, Int. J. Chem. Technol. 5 (2021) 33–41.
[5] N. Genli, S. Kutluay, O. Baytar, Ö. Şahin, Preparation and characterization of activated carbon from hydrochar by hydrothermal carbonization of chickpea stem: an application in methylene blue removal by RSM optimization, Int. J. Phytoremediat. 24 (2022) 88–100.
[6] S. Kutluay, O. Baytar, Ö. Şahin, A. Arran, Optimization of process conditions for adsorption of methylene blue on formaldehyde-modified peanut shells using Box-Behnken experimental design and response surface methodology, Eur. J. Tech. 10 (2020) 131–142.
[7] S. Kutluay, M.Ş. Ece, Ö. Şahin, Synthesis of magnetic Fe3O4/AC nanoparticles and its application for the removal of gas-phase toluene by adsorption process, Int. J. Chem. Technol. 4 (2020) 146–155.
[8] C. Saka, Ö. Şahin, S. Kutluay, Cold plasma and microwave radiation applications for surface modification on the pistachio husk-based adsorbent and its effects on the adsorption of rhodamine B, Energy Sour. Part A Recover. Util. Environ. Eff. 38 (2016) 339–346.
[9] C. da Luz, S.M. de Arruda Guelli Ulson de Souza, A.A. Ulson de Souza, A. Dervanoski, A. de Oliveira Samel Moraes, B.D. Wood, A multiscale model for carbon adsorption of BTX compounds: comparison of volume averaging theory and experimental measurements, Chem. Eng. Sci. 184 (2018) 285–308.
[10] B. Xiao, K. Thomas, Competitive adsorption of aqueous metal ions on an oxidized nanoporous activated carbon, Langmuir 20 (2004) 4566–4578.
[11] X. Yao, Y. Liu, T. Li, T. Zhang, H. Li, W. Wang, X. Shen, F. Qian, Z. Yao, Adsorption behavior of multicomponent volatile organic compounds on a citric acid residue waste-based activated carbon: experiment and molecular simulation, J. Hazard. Mater. 392 (2020), 122323.
[12] M.Ş. Ece, S. Kutluay, Ö. Şahin, S. Horoz, Development of novel Fe3O4/AC@SiO2@1,4-DAAQ magnetic nanoparticles with outstanding VOC removal capacity: characterization, optimization, reusability, kinetics, and equilibrium studies, Ind. Eng. Chem. Res. 59 (2020) 21106–21123.
[13] Ö. Şahin, S. Kutluay, S. Horoz, M.Ş. Ece, Fabrication and characterization of 3,4-diaminobenzophenone-functionalized magnetic nanoadsorbent with enhanced VOC adsorption and desorption capacity, Environ. Sci. Pollut. Res. 28 (2021) 5231–5253.
[14] M. de las Nieves Piña, P. Rodríguez, M.S. Gutiérrez, D. Quiñonero, J. Morey, A. Frontera, Adsorption and quantification of volatile organic compounds (VOCs) by using hybrid magnetic nanoparticles, Chem. Eur. J. 24 (2018) 12820–12826.
[15] R. Roto, Y. Yusran, A. Kuncaka, Magnetic adsorbent of Fe3O4@SiO2 core-shell nanoparticles modified with thiol group for chloroauric ion adsorption, Appl. Surf. Sci. 377 (2016) 30–36.
[16] J. Zhou, R. Li, S. Liu, Q. Li, L. Zhang, L. Zhang, J. Guan, Structure and magnetic properties of regenerated cellulose/Fe3O4 nanocomposite films, J. Appl. Polym. Sci. 111 (2009) 2477–2484.
[17] Q. Lu, Y. Zhang, H. Hu, W. Wang, Z. Huang, D. Chen, M. Yang, J. Liang, In situ synthesis of a stable Fe3O4@ cellulose nanocomposite for efficient catalytic degradation of methylene blue, Nanomaterials 9 (2019) 275.
[18] S. Kutluay, O. Baytar, Ö. Şahin, Equilibrium, kinetic and thermodynamic studies for dynamic adsorption of benzene in gas phase onto activated carbon produced from Elaeagnus angustifolia seeds, J. Environ. Chem. Eng. 7 (2019), 102947.
[19] Z. Zhao, S. Wang, Y. Yang, X. Li, J. Li, Z. Li, Competitive adsorption and selectivity of benzene and water vapor on the microporous metal organic frameworks (HKUST-1), Chem. Eng. J. 259 (2015) 79–89.
[20] K.S. Sing, R.T. Williams, Physisorption hysteresis loops and the characterization of nanoporous materials, Adsorpt. Sci. Technol. 22 (2004) 773–782.
[21] D. Saha, N. Mirando, A. Levchenko, Liquid and vapor phase adsorption of BTX in lignin derived activated carbon: equilibrium and kinetics study, J. Clean. Prod. 182 (2018) 372–378.
[22] H.-Y. Zhu, Y.-Q. Fu, R. Jiang, J.-H. Jiang, L. Xiao, G.-M. Zeng, S.-L. Zhao, Y. Wang, Adsorption removal of congo red onto magnetic cellulose/Fe3O4/activated carbon composite: equilibrium, kinetic and thermodynamic studies, Chem. Eng. J. 173 (2011) 494–502.
[23] X. Li, L. Zhang, Z. Yang, P. Wang, Y. Yan, J. Ran, Adsorption materials for volatile organic compounds (VOCs) and the key factors for VOCs adsorption process: a review, Sep. Purif. Technol. 235 (2020), 116213.
[24] A. Maleki, M. Kamalzare, Fe3O4@ cellulose composite nanocatalyst: preparation, characterization and application in the synthesis of benzodiazepines, Catal. Commun. 53 (2014) 67–71.
[25] A. Azizi, Green synthesis of Fe3O4 nanoparticles and its application in preparation of Fe3O4/cellulose magnetic nanocomposite: a suitable proposal for drug delivery systems, J. Inorg. Organomet. Polym. Mater. 30 (2020) 3552–3561.
[26] M.Ş. Ece, A. Ekinci, S. Kutluay, Ö. Şahin, S. Horoz, Facile synthesis and comprehensive characterization of Ni-decorated amine groups-immobilized Fe3O4@SiO2 magnetic nanoparticles having enhanced solar cell efficiency, J. Mater. Sci. Mater. Electron. 32 (2021) 18192–18204.
[27] S. Kutluay, Excellent adsorptive performance of novel magnetic nano-adsorbent functionalized with 8-hydroxyquinoline-5-sulfonic acid for the removal of volatile organic compounds (BTX) vapors, Fuel 287 (2021), 119691.
[28] S. Kutluay, S. Horoz, Ö. Şahin, A. Ekinci, M.Ş. Ece, Highly improved solar cell efficiency of Mn-doped amine groups-functionalized magnetic Fe3O4@SiO2 nanomaterial, Int. J. Energy Res. 45 (2021) 20176–20185.
[29] B. Rubahamya, K.S.K. Reddy, A.A. Shoaibi, C. Srinivasakannan, Porous carbon nitrification process optimization for enhanced benzene adsorption, Fuller. Nanotub. Carbon Nanostruct. 26 (2018) 16–22.
[30] Q. Zhou, Y. Wang, J. Xiao, H. Fan, Adsorption and removal of bisphenol A, α-naphthol and β-naphthol from aqueous solution by Fe3O4@ polyaniline core–shell nanomaterials, Synth. Met. 212 (2016) 113–122.
[31] S. Tural, M.Ş. Ece, B. Tural, Synthesis of novel magnetic nano-sorbent functionalized with N-methyl-D-glucamine by click chemistry and removal of boron with magnetic separation method, Ecotoxicol. Environ. Saf. 162 (2018) 245–252.
[32] M.Ş. Ece, Synthesis and characterization of activated carbon supported magnetic nanoparticles (Fe3O4/AC@SiO2@Sulfanilamide) and its application in removal of toluene and benzene, Colloids Surf. A Physicochem. Eng. Asp. 617 (2021), 126231.
[33] O. Baytar, Ö. Şahin, S. Horoz, S. Kutluay, High-performance gas-phase adsorption of benzene and toluene on activated carbon: response surface optimization, reusability, equilibrium, kinetic, and competitive adsorption studies, Environ. Sci. Pollut. Res. 27 (2020) 26191–26210.
[34] H.A. Maitlo, K.-H. Kim, A. Khan, J.E. Szulejko, J.C. Kim, H.N. Song, W.-S. Ahn, Competitive adsorption of gaseous aromatic hydrocarbons in a binary mixture on nanoporous covalent organic polymers at various partial pressures, Environ. Res. 173 (2019) 1–11.
[35] X. Zhang, B. Gao, A.E. Creamer, C. Cao, Y. Li, Adsorption of VOCs onto engineered carbon materials: a review, J. Hazard. Mater. 338 (2017) 102–123.
[36] L. Zhu, D. Shen, K.H. Luo, A critical review on VOCs adsorption by different porous materials: species, mechanisms and modification methods, J. Hazard. Mater. (2020), 122102.
[37] S. Kim, N.K. Gupta, J. Bae, K.S. Kim, Structural variations and generation of binding sites in Fe-loaded ZSM-5 and silica under the effect of UV-irradiation and their role in enhanced BTEX abatement from gas streams, J. Hazard. Mater. 384 (2020), 121274.
[38] L. Zhu, D. Shen, K.H. Luo, A critical review on VOCs adsorption by different porous materials: species, mechanisms and modification methods, J. Hazard. Mater. 389 (2020), 122102.
[39] A. Kumar, E. Singh, A. Khapre, N. Bordoloi, S. Kumar, Sorption of volatile organic compounds on non-activated biochar, Bioresour. Technol. 297 (2020), 122469.
[40] K.N. Gupta, N.J. Rao, G.K. Agarwal, Gaseous phase adsorption of volatile organic compounds on granular activated carbon, Chem. Eng. Commun. 202 (2015) 384–401.
[41] Y. Shen, N. Zhang, Facile synthesis of porous carbons from silica-rich rice husk char for volatile organic compounds (VOCs) sorption, Bioresour. Technol. 282 (2019) 294–300.
[42] X. Zhang, Y. Yang, L. Song, J. Chen, Y. Yang, Y. Wang, Enhanced adsorption performance of gaseous toluene on defective UiO-66 metal organic framework: equilibrium and kinetic studies, J. Hazard. Mater. 365 (2019) 597–605.
[43] L. Yu, L. Wang, W. Xu, L. Chen, M. Fu, J. Wu, D. Ye, Adsorption of VOCs on reduced graphene oxide, J. Environ. Sci. 67 (2018) 171–178.
[44] H. Sui, H. Liu, P. An, L. He, X. Li, S. Cong, Application of silica gel in removing high concentrations toluene vapor by adsorption and desorption process, J. Taiwan Inst. Chem. Eng. 74 (2017) 218–224.
[45] Y. Li, J. Miao, X. Sun, J. Xiao, Y. Li, H. Wang, Q. Xia, Z. Li, Mechanochemical synthesis of Cu-BTC@ GO with enhanced water stability and toluene adsorption capacity, Chem. Eng. J. 298 (2016) 191–197.
[46] Z.-Y. Gu, D.-Q. Jiang, H.-F. Wang, X.-Y. Cui, X.-P. Yan, Adsorption and separation of xylene isomers and ethylbenzene on two Zn− terephthalate metal− organic frameworks, J. Phys. Chem. C 114 (2010) 311–316.
[47] M.P. Nicolau, P.S. Bárcia, J.M. Gallegos, J.A. Silva, A.E. Rodrigues, B. Chen, Single- and multicomponent vapor-phase adsorption of xylene isomers and ethylbenzene in a microporous metal− organic framework, J. Phys. Chem. C 113 (2009) 13173–13179.
[48] F. Qu, L. Zhu, K. Yang, Adsorption behaviors of volatile organic compounds (VOCs) on porous clay heterostructures (PCH), J. Hazard. Mater. 170 (2009) 7–12.
[49] K. Yang, Q. Sun, F. Xue, D. Lin, Adsorption of volatile organic compounds by metal–organic frameworks MIL-101: influence of molecular size and shape, J. Hazard. Mater. 195 (2011) 124–131.
[50] H. Zaitan, D. Bianchi, O. Achak, T. Chafik, A comparative study of the adsorption and desorption of o-xylene onto bentonite clay and alumina, J. Hazard. Mater. 153 (2008) 852–859.
[51] M. Zhu, K. Zhou, X. Sun, Z. Zhao, Z. Tong, Z. Zhao, Hydrophobic N-doped porous biocarbon from dopamine for high selective adsorption of p-Xylene under humid conditions, Chem. Eng. J. 317 (2017) 660–672.
[52] H. Freundlich, Over the adsorption in solution, J. Phys. Chem. 57 (1906) 1100–1107.
[53] A. Sari, M. Tuzen, D. Citak, M. Soylak, Equilibrium, kinetic and thermodynamic studies of adsorption of Pb (II) from aqueous solution onto Turkish kaolinite clay, J. Hazard. Mater. 149 (2007) 283–291.
[54] A. Aziz, M. Kim, S. Kim, K.S. Kim, Adsorption and kinetic studies of volatile organic compounds (VOCs) on seed assisted template free ZSM-5 zeolite in air, J. Nanotechnol. Adv. Mater. 5 (2017) 1–9.
[55] S. Kutluay, F. Temel, Silica gel based new adsorbent having enhanced VOC dynamic adsorption/desorption performance, Colloids Surf. A Physicochem. Eng. Asp. 609 (2021), 125848.
[56] M.H.A. Azqhandi, M. Foroughi, E. Yazdankish, A highly effective, recyclable, and novel host-guest nanocomposite for Triclosan removal: a comprehensive modeling and optimization-based adsorption study, J. Colloid Interface Sci. 551 (2019) 195–207.

[57] S.N. Kudahi, A.R. Noorpoor, N.M. Mahmoodi, Determination and analysis of CO_2 capture kinetics and mechanisms on the novel graphene-based adsorbents, J. CO2 Util. 21 (2017) 17–29.
[58] G. Song, X. Zhu, R. Chen, Q. Liao, Y.-D. Ding, L. Chen, An investigation of CO_2 adsorption kinetics on porous magnesium oxide, Chem. Eng. J. 283 (2016) 175–183.
[59] N. Álvarez-Gutiérrez, M. Gil, F. Rubiera, C. Pevida, Kinetics of CO_2 adsorption on cherry stone-based carbons in CO_2/CH4 separations, Chem. Eng. J. 307 (2017) 249–257.
[60] N.A. Rashidi, S. Yusup, A. Borhan, L.H. Loong, Experimental and modelling studies of carbon dioxide adsorption by porous biomass derived activated carbon, Clean Technol. Environ. Policy 16 (2014) 1353–1361.
[61] M.A. Fulazzaky, M.H. Khamidun, R. Omar, Understanding of mass transfer resistance for the adsorption of solute onto porous material from the modified mass transfer factor models, Chem. Eng. J. 228 (2013) 1023–1029.
[62] B. Sadeghalvad, A. Azadmehr, A. Hezarkhani, Enhancing adsorptive removal of sulfate by metal layered double hydroxide functionalized Quartz-Albitophire iron ore waste: preparation, characterization and properties, RSC Adv. 6 (2016) 67630–67642.
[63] Y. Wang, H. Tao, D. Yu, C. Chang, Performance assessment of ordered porous electrospun honeycomb fibers for the removal of atmospheric polar volatile organic compounds, Nanomaterials 8 (2018) 350.
[64] K.Y. Foo, B.H. Hameed, Insights into the modeling of adsorption isotherm systems, Chem. Eng. J. 156 (2010) 2–10.
[65] C. Wang, H. Zhong, W. Wu, C. Pan, X. Wei, G. Zhou, F. Yang, Fe3O4@ C core–shell carbon hybrid materials as magnetically separable adsorbents for the removal of dibenzothiophene in fuels, ACS Omega 4 (2019) 1652–1661.
[66] W. Zou, B. Gao, Y.S. Ok, L. Dong, Integrated adsorption and photocatalytic degradation of volatile organic compounds (VOCs) using carbon-based nanocomposites: a critical review, Chemosphere 218 (2019) 845–859.
[67] F. Gan, B. Cheng, Z. Jin, Z. Dai, B. Wang, L. Yang, X. Jiang, Hierarchical porous biochar from plant-based biomass through selectively removing lignin carbon from biochar for enhanced removal of toluene, Chemosphere 279 (2021), 130514.
[68] M. Auta, B. Hameed, Adsorption of carbon dioxide by diethanolamine activated alumina beads in a fixed bed, Chem. Eng. J. 253 (2014) 350–355.